Materials Research. 2025; 28:e20240358
DOI: https://doi.org/10.1590/1980-5373-MR-2024-0358

Torsional Fatigue of Ti15Mo Titanium Alloy

***Wagner Pedro Hermes*[a], *Tatiane Haskel*[a], *Athos Henrique Plaine*[a]*, *Renato Barbieri*[a]**

[a]*Universidade do Estado de Santa Catarina (UDESC), Departamento de Engenharia Mecânica, Rua Paulo Malschitzki, 200, 89219-710, Joinville, SC, Brasil.*

Received: August 20, 2024; Revised: December 26, 2024; Accepted: February 13, 2025

This study investigates the torsional fatigue behavior of Ti-15Mo alloy through comprehensive analyses of its mechanical properties, microstructure, fatigue stress-life curves, and fracture surfaces, providing valuable insights into its fatigue characteristics. The hot-forged and air-cooled Ti15Mo alloy exhibited a microstructure predominantly consisting of equiaxial β phase grains, deformation twins, and ω athermal phase. Mechanical testing revealed a microhardness of 347.4 HV, yield and ultimate tensile strengths of 873 MPa, elongation of 20.7%, Young's modulus of 83.7 GPa, ultimate shear strength of 673 MPa, shear modulus of 30.5 GPa, and a fatigue strength limit of 190.2 MPa, as estimated by Basquin's model at 5 x 10^6 cycles. Fracture analysis indicated that crack nucleation predominantly occurred on the surface under pure torsion loading. In high-cycle fatigue (HCF) tests, cracks propagated at approximately 45° (Mode I), while in low-cycle fatigue (LCF) tests, propagation occurred at around 90° (Mode III). Fracture profiles also revealed significant number of deformation twins and instances of intragranular fracture near the fracture surface.

Keywords: *Ti-15Mo, Torsional fatigue, Mechanical properties, Microstructure, Fracture.*

1. Introduction

β-metastable titanium alloys are widely utilized across various industrial sectors, including aerospace, biomedical devices, and automotive industry, due to their exceptional combination of mechanical strength, fatigue resistance, corrosion resistance, and toughness[1-3]. In recent years, these alloys have gained significant attention in the biomedical field as implant materials because of their excellent biocompatibility, superior mechanical properties, lightweight nature, remarkable corrosion resistance, and non-magnetic characteristics[4,5]. To ensure the longevity of implants and minimize the need for revision surgeries, it is crucial to select materials with high strength, low modulus, and superior stability, making β-phase stabilized Ti alloys the preferred choice[6].

Among the elements that stabilize the β-phase, molybdenum (Mo) stands out as a robust candidate due to its complete solubility in titanium alloys, which enhances coherency, improves mechanical strength[5], reduces Young's modulus, and enhances corrosion resistance[7]. Numerous researchers, including Mohan et al.[5], have reported significant improvements in these properties and biocompatibility upon incorporating Mo into Ti-alloys.

Of particular interest is the binary Ti–15Mo alloy, renowned for its metastable β-phase, low elastic modulus, non-toxic composition, and excellent balance between strength and elasticity[8-10]. However, the mechanical properties of metastable β titanium alloys are highly influenced by thermomechanical processing, which induces phase transformations. Optimal mechanical properties are achieved in Ti alloys featuring a β-phase matrix with α-phase precipitates, while the presence of metastable ω-phase is considered undesirable[11]. These alloys exhibit a nuanced interplay of mechanical properties and deformation mechanisms that are sensitive to β-stability, including stress-induced phase transformations, mechanical twinning, and dislocation slip[3,12].

Fatigue, a common mode of failure in metals, significantly contributes to orthopedic implant failure, highlighting the importance of evaluating the fatigue strength and mechanical properties of Ti-based alloys. Understanding the fatigue behavior of β-type titanium alloys is essencial for predicting implant durability and ensuring safety during service[13]. While previous studies have primarily focused on the tensile or compressive strength and elastic modulus of Ti-15Mo alloys, there is limited research on their behavior under torsional fatigue loads[14]. Gatina et al.[15] investigated the uniaxial fatigue behavior and fracture features of Ti-15Mo alloy in the initial coarse-grained (α + β)-, single-phase coarse-grained β-, and ultrafine-grained (α + β)-states. Campanelli et al.[16] examined the role of twinning and nano-crystalline ω-phase on the uniaxial fatigue behavior of Ti-15Mo. Sugano et al.[17] studied the micromechanisms of plane bending fatigue fractures in Ti-15Mo and Ti-17Mo alloys using optical and electron microscopy.

This study aims to investigate the torsional fatigue behavior of the Ti-15Mo alloy (β-type), providing comprehensive insights derived from laboratory experiments[18]. The analyses include tensile and torsion mechanical properties, microstrucure analysis, torsional fatigue stress-life curve spanning from 10^3 to 10^7 cycles, macroscopic pattern of failures, comparison

*e-mail: athos.plaine@udesc.br

with established fatigue models, and profile and fracture surface analysis, shedding light on the alloy's torsional fatigue characteristics.

2. Materials and Methods

2.1. Material characterization

The specimens used in this study were manufactured from hot-forged (900°C) β-metastable Ti-15Mo alloy bars with a diameter of 9.3 mm, produced at the Aeronautic Technological Institute (ITA) in Brazil. The chemical composition of the alloy is presented in Table 1.

For metallographic analyses, two transverse section specimens and one longitudinal specimen, each with a thickness of 5 mm, were cut from the bars using a refrigerated cutting disc. Conventional metallography techniques, including grinding, polishing, and chemical etching with Kroll's solution, were subsequently applied. The microstructure was examined using an Olympus CX31 optical microscope (OM), and grain sizes were determined using the intercept method in accordance with ASTM E112 standard procedures[19].

X-ray diffraction (XRD) analysis was performed using a Shimadzu LabX XRD6000 diffractometer with Cu Kα radiation (λ = 0.15406 nm). Scanning was conducted at a speed of 1°/min over a range of $20° \leq 2\theta \leq 100°$, with a voltage of 40 kV and a current of 30 mA. Phase identification was carried out by matching diffraction patterns obtained from the Inorganic Crystal Structure Database (ICSD) using X'Pert software.

2.2. Mechanical characterization

Microhardness testing was conducted using a Shimadzu microhardness tester equipped with a Vickers indenter and a load of 0.5 kgf (HV 0.5). Each impression was subjected to a load application time of approximately 10 seconds, and five measurements were taken on each specimen.

Solid specimens with circular cross-sections were machined in accordance with ASTM standards (E8/E8M, E588-83, E606, and ISO 1352) to perform tensile, torsion, and torsional fatigue tests, as depicted in Figure 1. Prior to testing, the torsional fatigue specimens underwent surface finishing using progressively finer grades of silicon carbide-impregnated paper (400 to 2500 mesh) and polishing, resulting

Table 1. Chemical composition of the Ti15Mo alloy studied.

	Ti (wt.%)	Mo (wt.%)	Fe (wt.%)	H(ppt)	O (wt.%)	N(ppt)
Ti15Mo	-	15.7	0.04	154	0.15	44

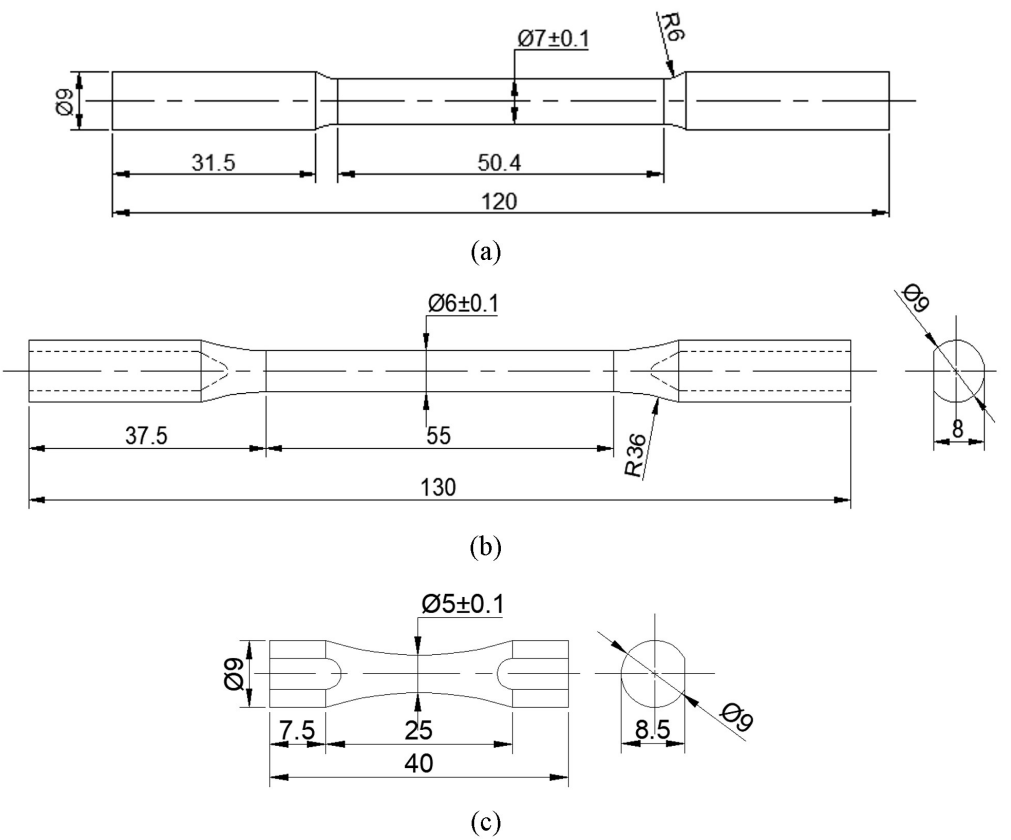

Figure 1. Solid specimens for (a) tensile tests (b) monotonic torsion tests (c) torsional fatigue tests (dimensions in mm).

in a surface roughness mean value (Ra) of approximately 0.118 ± 0.09 μm, well below the recommended 0.2 μm threshold specified by the ASTM E606 standard[20].

Tensile tests were conducted using an EMIC DL30 KN universal testing machine, with a displacement speed of 1 mm/min at room temperature, in accordance to ASTM E8/E8M-16a standard specifications[21]. Strains were measured using an EE10 NO 11645 model extensometer with a 25 mm opening, and yield strength was determined using the 0.2% offset method for axial deformation. Additionally, maximum elongation (%) was calculated based on two marks placed on the test specimen gauge region, and the extensometer was removed post-test to prevent damage.

Monotonic (quasi-static) torsion tests were performed at room temperature following ASTM E588-83[22] standard guidelines, utilizing a torsion testing machine with a maximum capacity of 75 Nm. Torque measurement was indirectly conducted using a reaction torquemeter built with a full Wheatstone bridge, while the motor shaft rotation angle and specimen torsion angle were measured using precision multi-turn potentiometers and a speed reducer reduction ratio of 1:40, respectively.

Torsional fatigue tests were conducted in accordance with ASTM E606 standard specifications[20], with failure occurring within the range of 3×10^3 to 10^7 cycles. Testing was performed using a machine based on the Scotch Yoke mechanism (see Figure 2), operating under strain-controlled conditions with stress ratio (R) of -1, frequency (f) of 10 Hz, and replication rate of 48%, at room temperature. Torque measurement was indirectly performed using a load cell, and the relationship between motor rotation angle (θ) and specimen twist angle (ϕ) was determined by Equation 1:

$$\tan(\phi) = \left(\frac{\text{Re x } \sin(\theta)}{\text{L} - \text{Re x } \cos(\theta)} \right) \quad (1)$$

where Re indicates the adjusted eccentricity value for each test and L is the distance between the motor center rotation and the specimen.

During fatigue tests, torque values were recorded at each time interval (Δt), and a 10% drop in the mean torque peak value was used as the criterion to determine failure torque (Tf) and the number of cycles to failure (N_f). Additionally, a procedure was implemented to evaluate the mechanical behavior of the alloy under higher torques. In this procedure, the hysteresis loop at mid-cycle was analyzed, and the hypothesis of linear material behavior was adopted based on the nearly closed shape of the hysteresis curve. The stress on the free surface of the specimen in the higher-torque region was calculated using Equation 2[23]:

$$\tau_a = 16.T_a / \left(\pi.d^3 \right) \quad (2)$$

where τ_a represents the shear stress amplitude (or alternating shear stress), T_a is the value of the alternating torque (value that coincides with torque in failure T_f for tests with R=-1) and d is the diameter of the specimen in the central section.

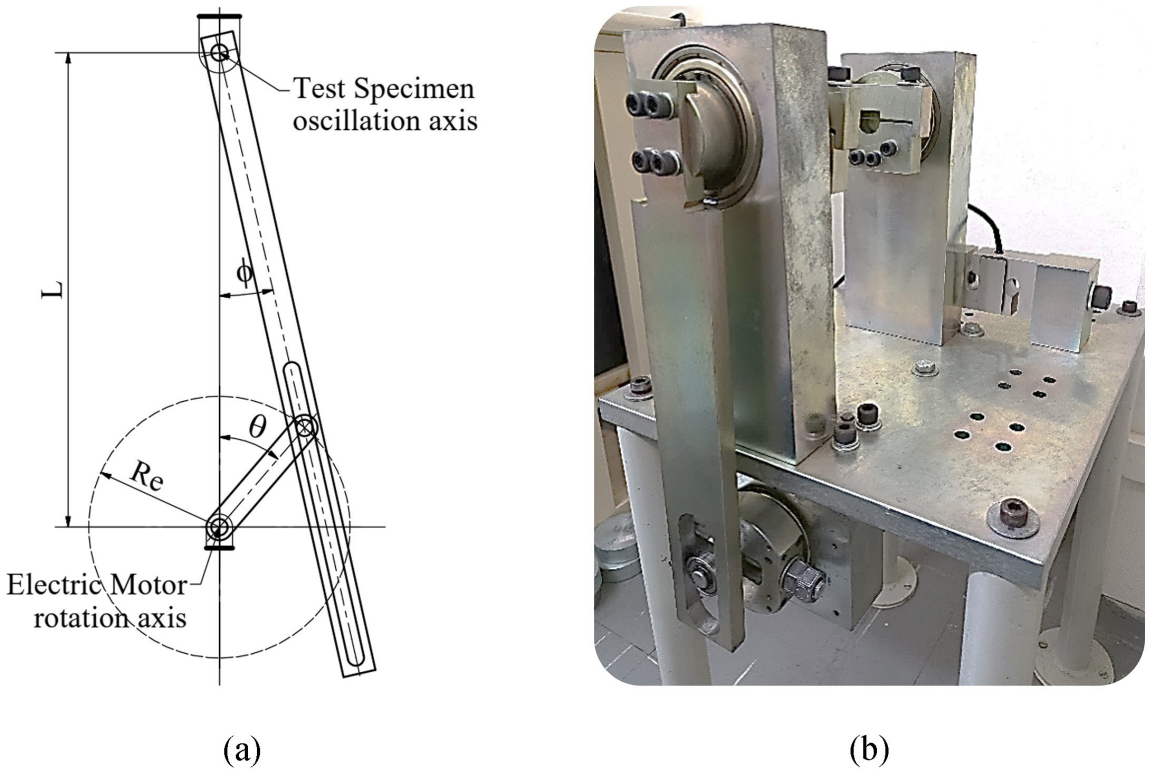

Figure 2. (a) Illustration of mechanism known as Scotch Yoke. (b) Torsional fatigue machine used in this study.

2.3. Fracture analysis

Fractured fatigue specimens were examined using confocal microscope (LEICA MZ9s) and field-emission scanning electron microscope (JSM-6701F JEOL) with magnification ranging from 25x to 1000x. The macroscopic fracture angles of the specimens were measured from the fracture images using the IC Measure software.

3. Results and Discussions

3.1. Material characterization

Figure 3a depicts the microstructure of the Ti15Mo alloy in its as-received condition, following hot forging and air cooling. The microstructure predominantly consists of equiaxed grains of the β phase, accompanied by twins. These twins are identified as deformation twins formed during the mechanical processing of the alloy bars. Similar observations of deformation twins and athermal ω nanocrystalline phases have been reported in previous studies of Ti15Mo alloy by Campanelli et al.[16] and Freitas[24]. Furthermore, irregularly shaped grains are evident in Figure 3a, a characteristic feature of materials subjected to thermomechanical processing, with an average grain size of 83.5 ± 2.5 μm. This grain morphology suggests the alloy's readiness for further mechanical and thermal treatments to tailor its properties for specific applications.

Figure 3b) displays the diffractogram of the Ti15Mo alloy, revealing the presence of β and athermal ω phases. The athermal ω phase may form from the β-phase through a purely displacive mechanism (diffusionless transformation)[25,26]. During non-equilibrium processes, such as quenching, the β phase can decompose into metastable phases, including α', α'', and ω, which act as intermediate phases in the β→α transformation[27]. These metastable phases play a crucial role in determining the alloy's mechanical and thermal behavior, warranting further investigation into their transformation kinetics and their effects on alloy's properties.

The Vickers microhardness mean value measured across the cross-section of the specimens was 347.4 ± 21.5 HV. The tensile test results for the Ti15Mo alloy, hot forged at 900°C and air-cooled, are summaruzed in Table 2. The yield strength was 873 ± 8 MPa, ultimate tensile strength was 873 ± 6 MPa, Young's modulus was 83.7 GPa, and elongation was 20.7 ± 2.6%. According to previous studies[27-29], the formation of the brittle ω phase typically increases yield strength while reducing ductility.

The shear modulus G and Poisson's ratio (υ) were estimated from the linear portion of the torque (T) versus twist angle (ϕ) curve obtained in the monotonic torsion test, using Equations 3 and 4. The determined values for these parameters were G = 30.5 GPa and υ = 0.357. The shear stress in the elastic region exhibited a linear variation with respect to the radius. However, the values of G and υ were estimated because it is not possible to accurately detect the onset of yielding in solid specimens from the T × ϕ curve. The central region of the specimen remained elastic, while yielding occurred in the outer region[30].

$$G = (\Delta T / \Delta\phi)\, x\, \left(L / J\right) \tag{3}$$

where L is the gauge length and J is the inertia polar moment.

$$G = E / \left[2\left(1+\upsilon\right)\right] \tag{4}$$

where the elasticity modulus E was obtained in the tensile test.

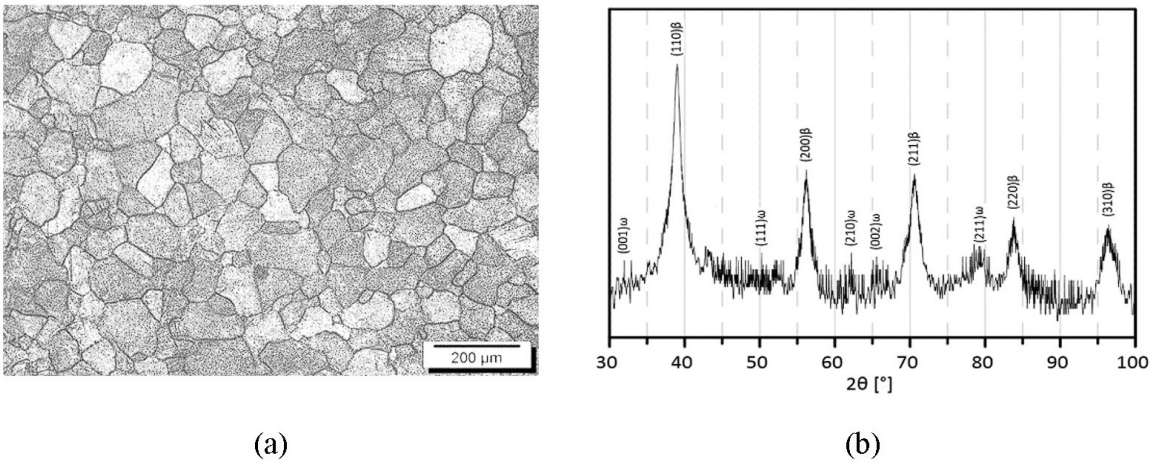

Figure 3. (a) Microstructure and (b) XRD spectrum of the as-received Ti15Mo alloy.

Table 2. Mechanical properties of Ti15Mo alloy.

Condition	Yield Strength, σ_y (MPa)	Tensile Strength, σ_{ut} (MPa)	Elongation (%)	E(GPa)	RA [%]	Microhardness (HV)
Ti15Mo alloy as received	873±8	873±6	20.7±2.6	83.7	67±3	347.4 ± 21.5

To obtain more precise data on the alloy's yield strength, thin-walled tubular specimens are recommended due to the minimal stress variation along the tube wall[23,30,31]. However, tubular specimens are generally more challenging to manufacture, increasing fabrication costs and experimental complexity.

Post-yielding, torque increased asymptotically until reaching the maximum torque, continuing to deform until failure. The ultimate shear strength τ_{ut} = 673 ± 5 MPa was determined using Nadai's equation (Equation 5)[23].

$$\tau_{ut} = [3T + \phi dT / \underline{d\phi}] / 2\pi r_o^3 \quad (5)$$

where τ_{ut} is the ultimate shear strength, ϕ is the twist angle in ultimate shear strength, r_o is the test specimen external radius in gauge length and dT/dϕ ≅ 0 (asymptote).

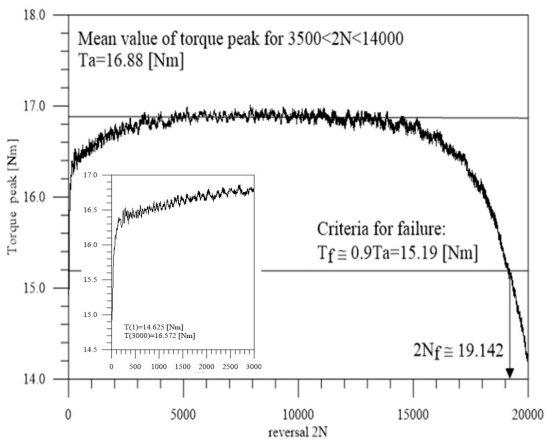

Figure 4. Torque peak history with failure at $2N_f$ = 19,142 cycles. Detail of the increase in torque in the initial cycles.

3.2. Torsional fatigue tests

Figure 4 illustrates the typical torque peak behavior observed during the tests and provides a detailed view of torque peaks at the onset of testing. Initially, torque increases rapidly over a few cycles. Subsequently, the torque peaks stabilize for most of the test duration, with a rapid drop near failure attributed to the nucleation and growth of fatigue cracks, consistent with findings from other studies[31-34].

Figure 5a shows the post-processing of a nearly stable loading and unloading cycle (half-lifetime hysteresis loop) for a test conducted with alternating torque of 17 Nm, oscillating between -6° and 6°, culminating in failure at N_f = 5,500 cycles. In this case, 266 data points captured a full cycle of motor axis movement, showing a nearly closed hysteresis curve. The fitted curve in Figure 5b indicates that the T x ϕ relationship remained nearly linear throughout the range of torsional angles, supporting the assumption of linear alloy behavior in this regime and the adoption of Equation 2 for shear stress amplitude estimation (as detailed in Section 2.2).

Figure 6 presents experimental results from torsional fatigue tests spanning 10^3 to 10^7 cycles, showing a decrease in stress amplitude with increasing cycles to failure (N_f). The Basquin equation ($\tau_a = \tau'_f \times N_f^{b\gamma}$) was used to fit the experimental data, yielding torsional fatigue strength coefficient (τ'_f) and exponent (b_γ) values of 2077.65 and -0.155, respectively. In the low-cycle fatigue (LCF) regime (~10^4 cycles), the alloy exhibited more dispersed behavior, with stress ranging from 450 to 650 MPa, while fatigue life varied from 4,000 to 16,000 cycles. Above the yield stress in the plastic regime, the alloy's fatigue life significantly diminished[31,32].

Additionally, torsional fatigue test results were fitted using the Kohout-Věchet model[33], described by Equation 6:

$$\tau_a = \tau_1 \left[\left(1 + N_f / B\right) / \left(1 + N_f / C\right) \right]^{b_{KV}} \quad (6)$$

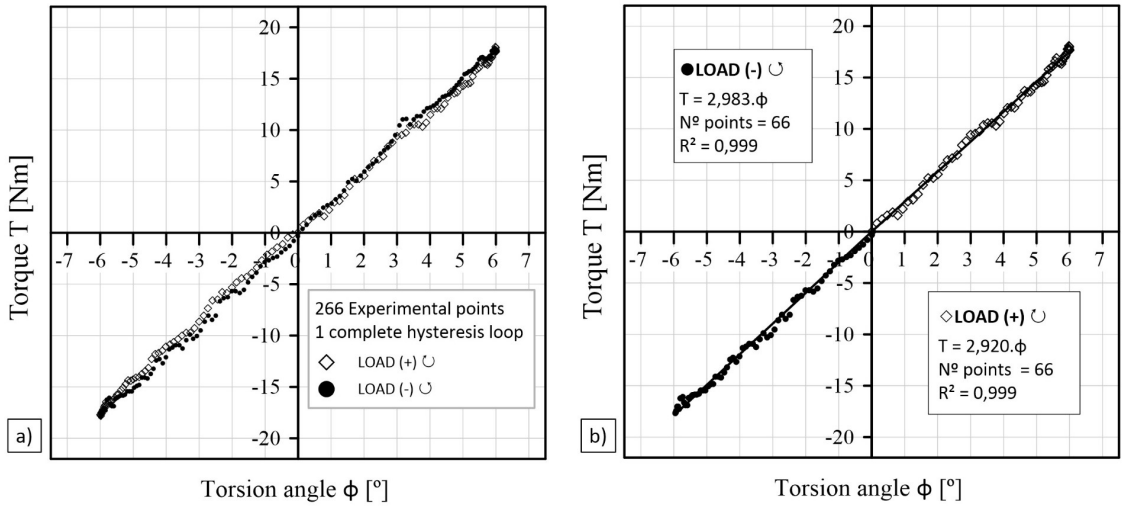

Figure 5. (a) Complete hysteresis cycle for a fatigue specimen subjected to high torque (N_f = 5,500 cycles) and (b) Half hysteresis cycle showing the linear relationship T x ϕ.

where τ_1 is the torsional fatigue strength coefficient, b_{KV} is the torsional fatigue strength exponent, B and C are constants.

Figure 6 also compares the application of the Kohout-Věchet model with Basquin's estimates. Parameters for both models were adjusted using the least squares method, resulting in determination coefficients $R^2 > 0.9$. τ_1, considered equivalent to alloy torsional strength by the Kohout-Věchet model, closely matched the monotonic torsion test result (τ_1 = 650 MPa and τ_{ut} = 673±5 MPa). It is recommended to perform fatigue tests in the low-cycle region ($N_f < 10^3$) to define a more accurate estimate for the τ_1 component, although the Kohout-Věchet model serves as an estimation criterion rather than defining alloy parameters and properties.

Moreover, there is a convergence between Basquin and Kohout-Věchet estimates within the range of 5 x 10^3 to 10^6 cycles, while divergence outside of this range was observed. The torsional fatigue strength exponents (b) for Basquin and Kohout-Věchet models were closely aligned at 0.155 and 0.164, respectively. Dieter[30] found torsional fatigue limits (S_{se}) of 195 MPa at 10^7 cycles from experimental data, whereas this study estimated S_{se} values of 190.2 MPa at 5 x 10^6 cycles using Basquin's model and 189.4 MPa at 10^8 cycles using Kohout-Věchet's model.

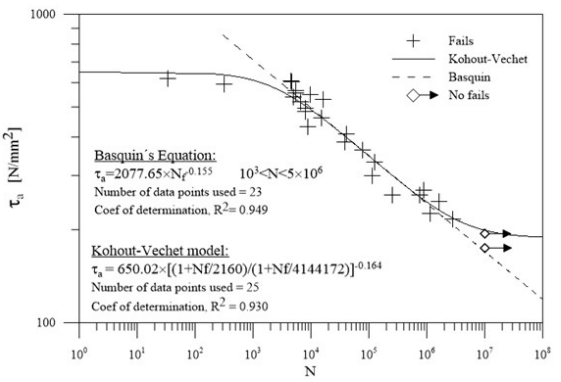

Figure 6. Comparison between Basquin and Kohout-Věchet estimates.

Table 3 summarizes these findings alongside the S_{se}/σ_{ut} ratio, while Table 4 compares the fatigue limits (S_e) between uniaxial and torsional fatigue under different alloy processing conditions. Torsional fatigue limits were lower compared to uniaxial fatigue limits, reflecting the alloy's reduced resistance to stress under torsional loading conditions[15,16].

Boyer et al.[35] suggested an empirical measure of engineering cyclic properties, with the endurance limit/ultimate tensile strength ratio S_e/σ_{ut} often exceeding 0.5. For the Ti-6Al-4V alloy featuring coarse grains, ratios around 0.6 were reported, contrasting with values around 0.4 for alloys with ultra-fine grains. Meggiolaro et al.[36] observed significant dispersion in axial fatigue limit (S_e/S_{ut}) values across titanium alloys, ranging from 0.1 to 0.8 depending on alloy and processing conditions. Niinomi[37] reported $S_e \approx 400$ MPa for Ti-15Mo-5Zr-3Al alloy without specifying conditions. Campanelli et al.[16] studied uniaxial fatigue for Ti-15Mo alloy using the staircase method, finding S_e values of 546 MPa for the as-received alloy (forged, annealed at 800°C, air-cooled) and 513 MPa for the alloy solubilized at 900°C and water-quenched, with corresponding σ_{ut} values.

In a recent publication[15], the influence of grain refinement on axial fatigue of Ti-15Mo alloy was highlighted. For Ti-15Mo(β) alloy with coarse grains (solubilized at 810°C, water-quenched), the experimental fatigue limit was 400 MPa (R = -1), with $S_e/\sigma_{ut} = 0.51$. Comparable values for Ti-15Mo (α + β) alloy with coarse grains were S_e = 500 MPa (R = -1) and $S_e/\sigma_{ut} = 0.49$, while ultra-refined grains yielded S_e = 710 MPa (R = -1) with $S_e/\sigma_{ut} = 0.45$.

Considering $S_{se} \approx 0{,}5S_e$ for estimates using the Tresca method and $S_{se} \cong 0{,}577S_e$ when the von Mises method is used, the presented values (Table 3) of 0.44 and 0.38, respectively, align well with previously cited research. Sharifimehr et al.[38] and Nikitin et al.[39] advocated for the von Mises criterion in titanium alloy estimates. However, the values for S_e and S_e/σ_{ut} in this study were lower when compared to other results[15,16] due to the alloy's reduced stress tolerance under torsional fatigue conditions. Experimental tests focused on this high-cycle region followed standard guidelines such as

Table 3. Ratio between the torsional fatigue limit S_{se} and the equivalent ultimate tension strength σ_{ut}.

Estimate	S_{se} [MPa]	S_{se}/σ_{ut}	Tresca $S_{se}/0.5\sigma_{ut}$	Von Mises $S_{se}/0.577\sigma_{ut}$
Basquin	190	0.22	0.44	0.38
Kohout-Věchet	189	0.22	0.44	0.38
Dieter	195	0.22	0.44	0.38

Table 4. Comparison between uniaxial and torsional fatigue limits (S_e).

Alloy	Fatigue Test	Alloy Processing	Microstructure	S_e [MPa]	S_e/σ_{ut}
Ti-15Mo (This study)	Torsional	Hot forged at 900°C, air cooled	-	190	0.22
Ti-15Mo[16]	Uniaxial	Forged, annealed 800°C, air cooled	-	546	-
Ti-15Mo[16]	Uniaxial	Solubilized at 900°C, water-quenched	-	513	-
Ti-15Mo[15]	Uniaxial	Solubilized at 810°C, water-quenched	coarse grains	400	0.51
Ti-15Mo[15]	Uniaxial	-	ultra-refined grains	710	0.45

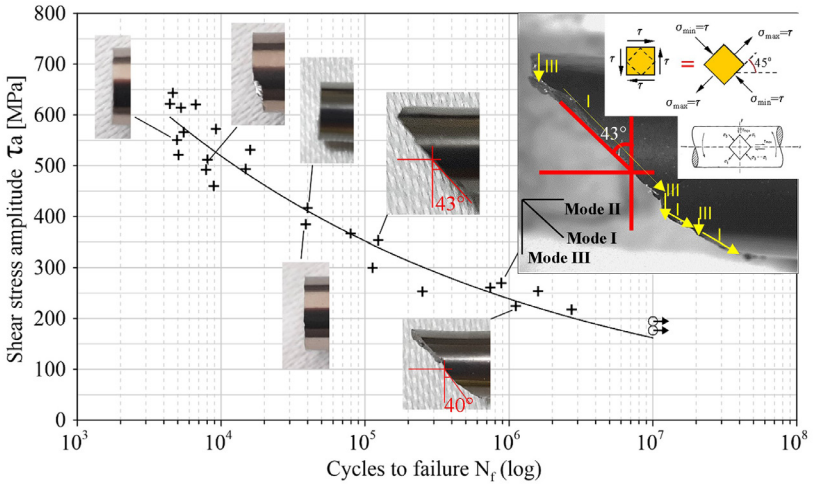

Figure 7. Macroscopic failure patterns as a function of stress amplitude and torsional fatigue life of Ti-15Mo alloy. Detail of the surface stress state and failure modes on the fracture surface of a specimen that failed near 10^6 cycles.

the staircase method[40], which is recommended for precise determination of alloy fatigue limits.

Figure 7 presents experimental results from torsional fatigue tests alongside the fitted Basquin curve and showcases macroscopic failure patterns based on shear stress amplitude levels. Figure 7 also illustrates stress states and failure modes on the fracture surface of a specimen that failed near 10^6 cycles, exhibiting mixed mode I and III crack propagation. Most specimens failing above 10^5 cycles displayed crack propagation at approximately 45° to the longitudinal axis, indicative of mode I crack propagation in high-cycle fatigue (HCF) tests. For $N_f < 10^5$ cycles, fractures generally occurred at approximately 90° to the longitudinal axis (flat fracture), characteristic of mode III crack propagation.

3.3. Fatigue fracture

3.3.1. Fracture in High-Cycle Fatigue (HCF) Tests ($N_f > 10^5$ cycles)

As discussed in Section 3.3, the majority of specimens in HCF tests exhibited a macroscopic fracture pattern at approximately 45º relative to the longitudinal axis. This pattern indicates that maximum tensile stresses (σ_1 and σ_3) predominantly governed crack propagation. These stresses are situated at a 45º angle from the plane of maximum shear stress induced by torque.

Figure 8a provides a detailed view of the fracture surface from a specimen that failed after N_f = 1,590,038 cycles. Fatigue cracks are observed radiating from a common point on the specimen's surface. (1) denotes probable sites of fatigue crack initiation, while (2) indicates macrocracks. The stable crack propagation zone exhibits typical cyclic crack growth features such as river patterns, striations, and propagation direction[16,32,41]. Studies and stress analyses have established that fatigue cracks initiate in planes of maximum shear stress and propagate under tensile stress along the material's crystalline structure. In pure torsion, shear stresses increase radially, with maximum values at the surface; thus, the surface becomes the preferred site for crack initiation[42].

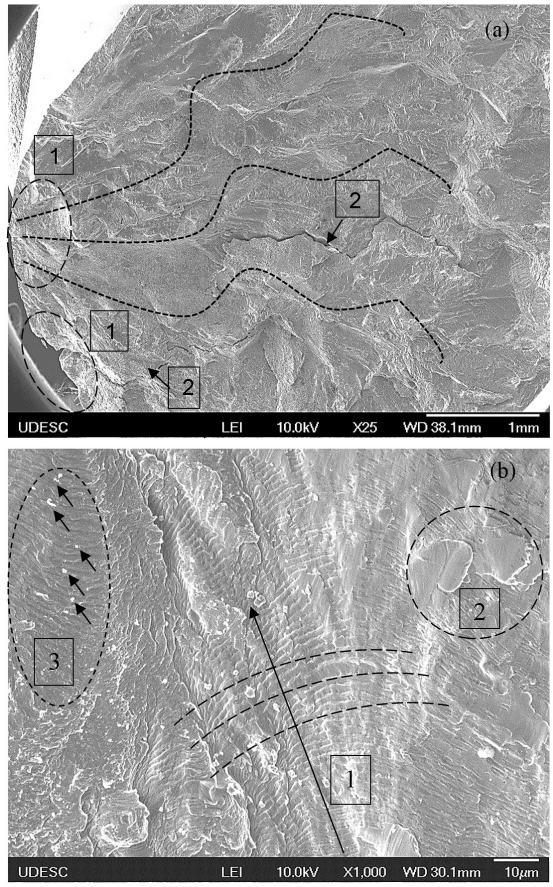

Figure 8. SEM fracture image of Ti15Mo alloy with N_f = 1,590,038 cycles: (a) fatigue crack nucleation site and (b) propagation.

Figure 8b, at higher magnification, reveals additional characteristics: (1) circumferential cyclic marks indicating crack propagation direction, (2) crumpled regions suggesting

abrasion and shear between crack edges within the torsion-loaded alloy[39], and (3) small particles likely resulting from such abrasion or specimen rupture.

Furthermore, microstructural profiles of specimens that fractured during HCF tests were analyzed. Figure 9 illustrates the microstructural fracture profile of a specimen with N_f = 132,466 cycles, showing an approximate fracture angle of 45º. Several distinct regions are identified for discussion. Region 1 (Figure 9b), near the fracture, exhibits refined grains with numerous deformation twins. Moving leftward towards the specimen's interior, region 2 shows a visible microstructural transition from the highly fatigued area (with increased twin density near the fracture) to a less affected region characterized by larger, more uniform grains predominantly composed of the β phase. Figure 9c provides a closer view of this transition. Campanelli et al.[16] also observed the development of deformation twins during fatigue testing. According to Qian et al.[43], mechanical twinning is primarily activated under conditions of enhanced β phase stability (equivalent to Mo content approximately between 12% and 15%). Min et al.[29] studied deformation mechanisms in hot-forged Ti–15Mo alloy during tensile tests, highlighting strain hardening induced by dynamic microstructural refinement via twinning.

Figure 10a presents a magnified image showing deformation twins near the fracture region. Researchers[16,17] have noted that the fatigue limit depends partly on the motion of dislocations hindered by twins, and largely on the presence of the nano-crystalline ω phase.

Fracture profiles also indicated instances of intragranular fracture. Figure 10b (an enlargement of Figure 9, Region 3) demonstrates a crack propagating through grains (grains fractured in half), typically associated with cleavage and brittle fracture behavior. Given that macrofractures occur around a 45º angle from the longitudinal axis, it is inferred that maximum tensile stresses predominantly govern crack propagation via Mode I.

3.3.2. Fracture in Low-Cycle Fatigue (LCF) Tests ($N_f < 10^5$ cycles)

Most of LCF specimens failed at approximately 90º relative to the longitudinal axis, which is attributed to maximum shear stresses induced by pure torsion loading. The SEM fractographic analysis of the fracture surface (Figure 11a) revealed several distinctive features: (1) macrocrack initiation at the specimen surface, where maximum shear stresses occur in pure torsion, followed by propagation through the specimen interior until final fracture at (2). Cyclic marks in the circumferential direction are evident across much of the fracture surface (3).

Figure 11b illustrates cyclic marks gradually increasing in spacing until reaching the final fracture region, characterized

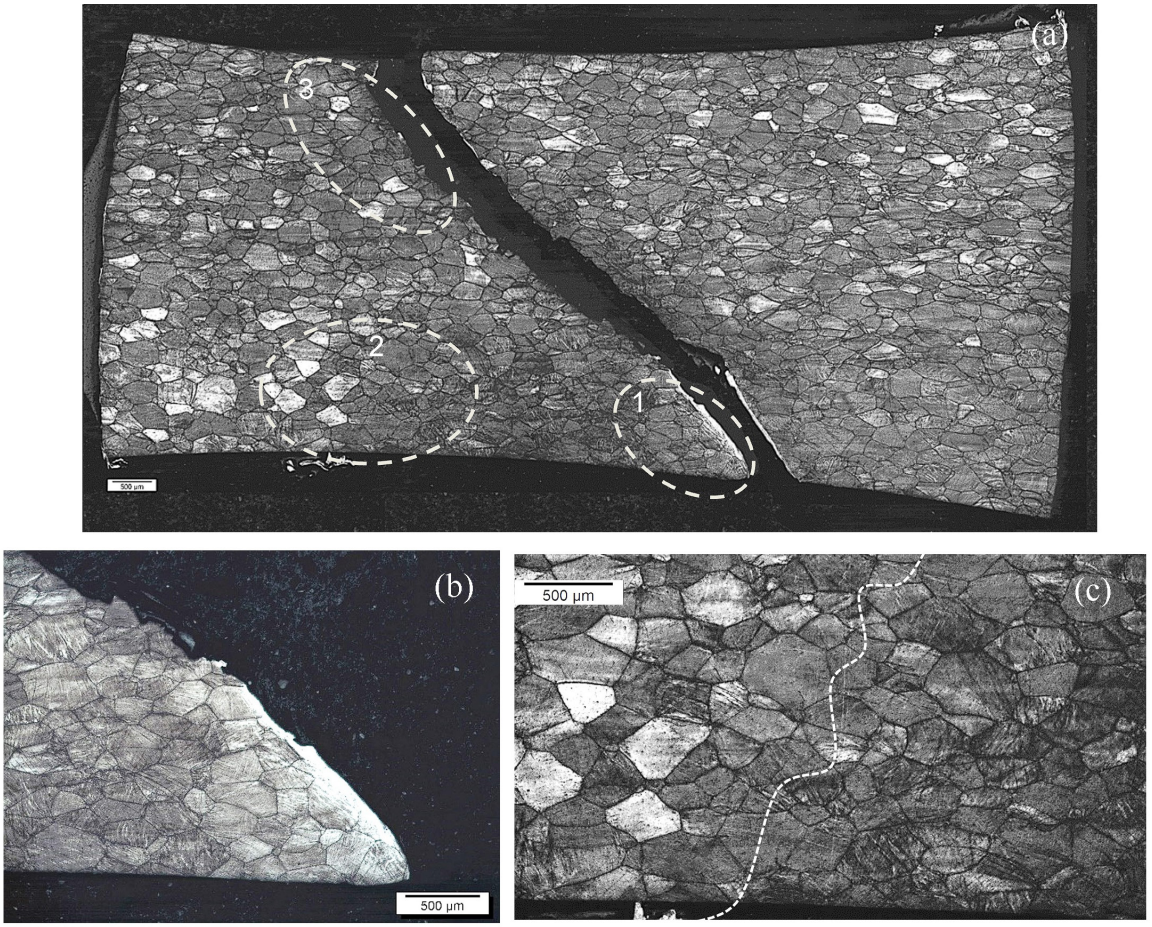

Figure 9. (a) Torsional fatigue fracture profile of Ti15Mo alloy (N_f = 132,466 cycles) and (b) and (c) higher magnification of regions 1 and 2.

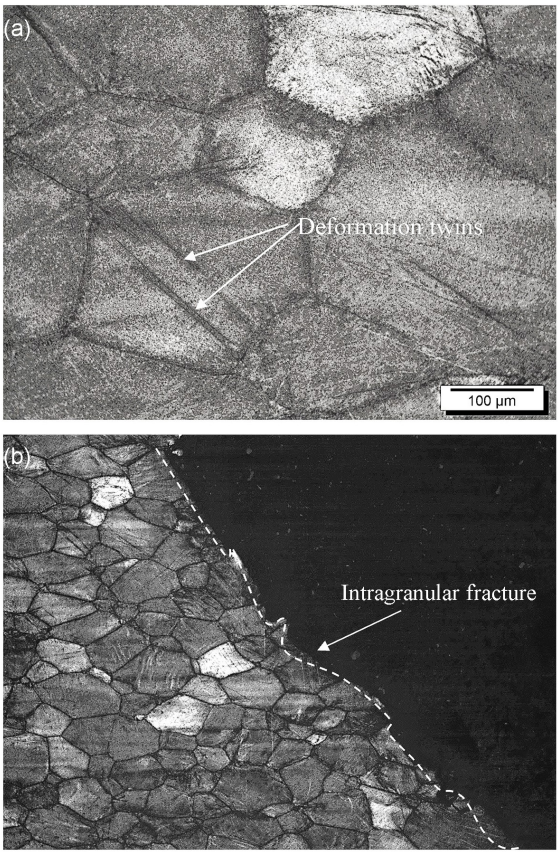

Figure 10. (a) Image highlighting the deformation twins close to the fracture and (b) Fracture profile showing evidence of intragranular fracture (N_f = 132,466 cycles).

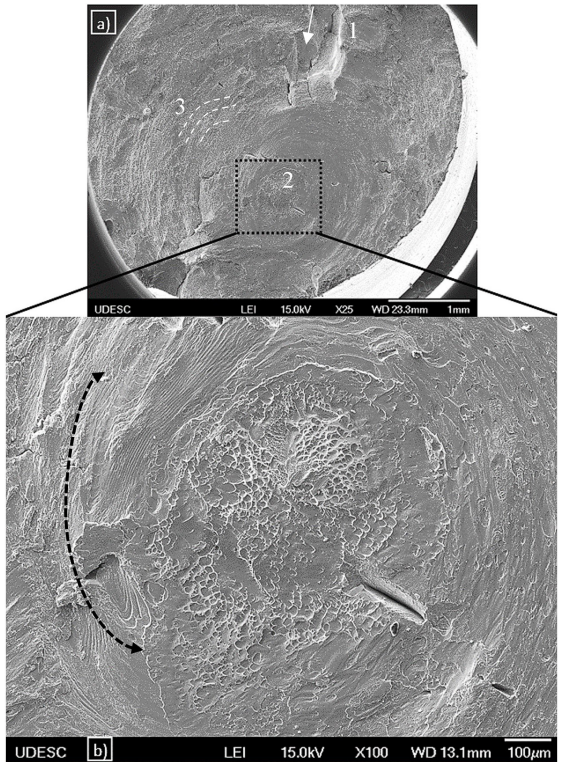

Figure 11. (a) Fatigue fracture SEM image in LCF test (N_f = 46,075 cycles) and b) arrow indicating the twist rotational direction.

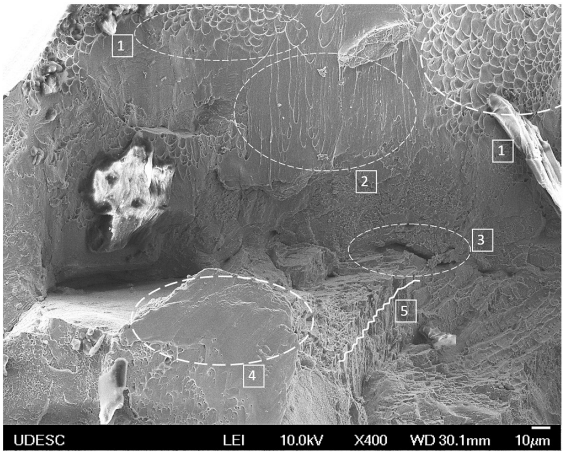

Figure 12. Details fractured specimen of Ti15Mo alloy with N_f = 8,883 cycles.

by concentrated dimples indicative of final rupture under tensile stresses. Azevedo et al.[44] also observed two distinct areas with cyclic marks and a central ductile fracture zone in their fracture surface analysis.

For a test specimen that fractured at N_f = 8883 cycles (Figure 12), crack nucleation occurred below the surface (subsurface), with visible river lines (macroscopic linear features radiating from the initiation site) extending to the central region of this area[32]. Campanelli et al.[16] observed that subsurface crack initiation in β alloys is uncommon, speculating that deformation twins induced by localized plastic deformation during fatigue testing may have facilitated abnormal crack nucleation. In Campanelli's study, crack initiation occurred at the twin plane following accumulation of helical dislocations along the twin boundary, which internally creating a stress concentrator. Fatigue failure manifests as a localized phenomenon rather than affecting the entire bulk material.

In the present study, the LCF test specimen exhibited crack propagation radiating from a common point in a plane approximately 90º relative to the longitudinal axis, where maximum shear stresses were active. The final rupture surface displayed a rough appearance, where crack propagation shifted to planes inclined at approximately 45º relative to the nucleation plane. This crack propagation exhibited a mixed mode, partly at 90º and partly at 45º relative to the longitudinal axis. The overload zone (final rupture) displayed characteristics of both ductile and brittle fracture, featuring rupture and cleavage planes. Similar observations were reported by other researchers[15]. Figure 12 provides detailed insights into the fracture region near the specimen surface, highlighting: (1) equiaxial dimples; indicative of microvoid formation under tensile stress without directional distortion, (2) elongated dimples characteristic of fracture surfaces subjected to pure shear, as typical in ductile metals under torsion[45]; (3) a surface

microcrack; (4) a smooth area indicating brittle fracture planes; and (5) stepwise crack propagation at approximately 45º and 90º angles along the fracture surface, associated with Modes I and III of crack propagation.

4. Conclusions

Based on the results and analyses presented in this paper concerning the microstructure, monotonic mechanical properties, torsional fatigue behavior, application and comparison of Basquin and Kohout-Věchet models on shear stress-life results, and torsional fracture surfaces of Ti15Mo alloy, the following conclusions can be drawn:

1) The microstructure of the hot-forged and air-cooled Ti15Mo alloy predominantly consists of equiaxial grains of the β phase, deformation twins (ω), and ω athermal phase.
2) Mechanical property characterization revealed a microhardness of 347.4 HV, yield strength and ultimate tensile strength of 873 MPa, elongation of 20.7%, Young's modulus of 83.7 GPa, ultimate shear strength of 673 MPa, shear modulus of 30.5 GPa, and a fatigue strength limit of 190.2 MPa estimated by Basquin's model at 5 x 10^6 cycles.
3) Estimates from both Basquin and Kohout-Věchet models for the shear stress-life curve converged within the range of 5x10^3 to 10^6 cycles. The fatigue strength exponents were determined as $b_{Basquin}$ = -0.155 and $b_{Kohout\text{-}Věchet}$ = -0.164.
4) Fracture analysis indicated that crack nucleation predominantly occurred on the surface (in both LCF and HCF tests), where maximum shear stresses are present under pure torsion loading. In HCF tests, crack propagation was predominantly governed by maximum tensile stresses and occurred at approximately 45° relative to the longitudinal axis (Mode I crack propagation). In LCF tests, crack propagation occurred at approximately 90° relative to the longitudinal axis (Mode III crack propagation), and final rupture was characterized by tensile rather than shear failure.
5) Microstructural fracture profiles revealed a higher number of deformation twins in regions near the fracture and instances of intragranular fracture.

5. Acknowledgments

This study was partly financed by The Santa Catarina Research Foundation (FAPESC) - Finance Code 2021TR001901; and partly by The National Council for Scientific and Technological Development (CNPq) - Finance Code 310995/2022-1.

6. References

1. Favre L, Mari D, Baluc N. Growth of α and ω phase in Ti4733 detected by mechanical spectroscopy. J Alloys Compd. 2023;955:170228. http://doi.org/10.1016/j.jallcom.2023.170228.
2. Veverková A, Kozlík J, Bartha K, Kosutová T, Correa CA, Becker H, et al. Preparation of bulk Ti–15Mo alloy using cryogenic milling and spark plasma sintering. Mater Charact. 2021;171:110762. http://doi.org/10.1016/j.matchar.2020.110762.
3. Zhang J, Sun F, Chen Z, Yang Y, Shen B, Li J, et al. Strong and ductile beta Ti–18Zr–13Mo alloy with multimodal twinning. Mater Res Lett. 2019;7(6):251-7. http://doi.org/10.1080/21663831.2019.1595763.
4. Cojocaru VD, Nocivin A, Trisca-Rusu C, Dan A, Irimescu R, Raducanu D, et al. Improving the mechanical properties of a β-type Ti-Nb-Zr-Fe-O alloy. Metals. 2020;10(11):1491. http://doi.org/10.3390/met10111491.
5. Mohan P, Rajak DK, Pruncu CI, Behera A, Amigó-Borrás V, Elshalakany AB. Influence of β-phase stability in elemental blended Ti-Mo and Ti-Mo-Zr alloys. Micron. 2021;142:102992. http://doi.org/10.1016/j.micron.2020.102992.
6. Gürgen S, Diltemiz SF, Kuşhan MC. Oxidation and thermal shock behavior of thermal barrier coated 18/10CrNi alloy with coating modifications. J Mech Sci Technol. 2017;31(1):149-55. http://doi.org/10.1007/s12206-016-1214-2.
7. Martins JRS Jr, Nogueira RA, Araújo RO, Donato TAG, Arana-Chavez VE, Claro PARA, et al. Preparation and characterization of Ti-15Mo alloy used as biomaterial. Mater Res. 2011;14(1):107-12. http://doi.org/10.1590/S1516-14392011005000013.
8. Xu H, Li Z, Yu L, Dong A, Xing H, Du D, et al. In-situ tailoring mechanical properties of metastable Ti15Mo alloy produced by selective laser. Mater Sci Eng A. 2023;863:144546. http://doi.org/10.1016/j.msea.2022.144546.
9. Verestiuc L, Spataru MC, Baltatu MS, Butnaru M, Solcan C, Sandu AV, et al. New Ti–Mo–Si materials for bone prosthesis applications. J Mech Behav Biomed Mater. 2021;113:104198. http://doi.org/10.1016/j.jmbbm.2020.104198.
10. Chen J, Li C, Zhou L, Ren Y, Li C, Liao X, et al. The anisotropic of corrosion and tribocorrosion behaviors of Ti–15Mo alloy fabricated by selective laser melting. Mater Charact. 2022;190:112000. http://doi.org/10.1016/j.matchar.2022.112000.
11. Bartha K, Stráský J, Veverková A, Veselý J, Janeček M. Observation of the omega phase particles in Ti15Mo alloy by electron microscopy. Mater Lett. 2022;309:131376. http://doi.org/10.1016/j.matlet.2021.131376.
12. Al-Zain Y, Sato Y, Kim HY, Hosoda H, Nam TH, Miyazaki S. Room temperature aging behavior of Ti–Nb–Mo-based superelastic alloys. Acta Mater. 2012;60(5):2437-47. http://doi.org/10.1016/j.actamat.2011.12.033.
13. Okazaki Y, Gotoh E. Comparison of fatigue strengths of biocompatible Ti-15Zr-4Nb-4Ta alloy and other titanium materials. Mater Sci Eng C. 2011;31(2):325-33. http://doi.org/10.1016/j.msec.2010.09.015.
14. Senopati G, Rahman Rashid RA, Kartika I, Palanisamy S. Recent development of low-cost β-Ti alloys for biomedical applications: a review. Metals. 2023;13(2):194. http://doi.org/10.3390/met13020194.
15. Gatina AS, Polyakova VV, Modina IM, Semenova IP. Fatigue behavior and fracture features of Ti-15Mo alloy in β-, (α + β)-, and ultrafine-grained two- phase states. Metals. 2023;13(3):580. http://doi.org/10.3390/met13030580.
16. Campanelli LC, Coury FG, Guo Y, Silva PSCP, Kaufman MJ, Bolfarini C. The role of twinning and nano-crystalline ω phase on the fatigue behavior of the metastable β Ti-15Mo alloy. Mater Sci Eng A. 2018;729:323-30. http://doi.org/10.1016/j.msea.2018.05.069.
17. Sugano M, Tsuchida Y, Satake T, Ikeda M. A microstructural study of fatigue fracture in titanium-molybdenum alloys. Mater Sci Eng A. 1998;243(1-2):163-8. http://doi.org/10.1016/S0921-5093(97)00795-8.
18. Hermes WP. Torsional fatigue of metastable β-type Ti15Mo titanium alloy [dissertation]. Joinville: Universidade do Estado de Santa Catarina; 2022.
19. ASTM: American Society for Testing and Materials. ASTM E112: standard test methods for determining average grain size. West Conshohocken: ASTM; 2021.

20. ASTM: American Society for Testing and Materials. ASTM E606: standard test method for strain-controlled fatigue testing. West Conshohocken: ASTM; 2021.
21. ASTM: American Society for Testing and Materials. ASTM E8/E8M-16a: standard test methods for tension testing of metallic materials. West Conshohocken: ASTM; 2020.
22. ASTM: American Society for Testing and Materials. ASTM E588-83. West Conshohocken: ASTM; 1983.
23. ASTM: American Society for Testing and Materials. ASTM E2207: standard practice for strain-controlled axial-torsional fatigue testing with thin-walled tubular specimens. West Conshohocken: ASTM; 2015.
24. Freitas MCRS. Caracterização da liga Ti-15Mo após tratamento termomecânico [dissertation]. São Paulo: Universidade de Taubaté; 2005.
25. Bartha K, Stráský J, Veverková A, Veselý J, Janeček M. Observation of the omega phase particles in Ti15Mo alloy by electron microscopy. Mater Lett. 2022;309:131376. http://doi.org/10.1016/j.matlet.2021.131376.
26. Veverková A, Harcuba P, Veselý J, Barriobero-Vila P, Doležal P, Pospíšil J, et al. Sequence of phase transformations in metastable β Zre12Nb alloy studied in situ by HEXRD and complementary techniques. J Mater Res Technol. 2023;23:5260-9. http://doi.org/10.1016/j.jmrt.2023.02.076.
27. Nag S. Influence of beta instabilities on the early stages of nucleation and growth of alpha in beta titanium alloys [thesis]. Ohio: Ohio State University; 2008.
28. Araújo RO. Influência do zircônio e do oxigênio na estrutura, microestrutura e propriedades mecânicas de ligas do sistema Ti-Mo-Zr [thesis]. Bauru: Universidade Estadual Paulista; 2017.
29. Min X, Chen X, Emura S, Tsuchiya K. Mechanism of twinning-induced plasticity in β -type Ti–15Mo alloy. Scr Mater. 2013;69(5):393-6. http://doi.org/10.1016/j.scriptamat.2013.05.027.
30. Dieter GE. Mechanical metallurgy. Boston: McGraw-Hill; 1986.
31. Betemps MI, Haskel T, Barbieri R, Verran GO. Effect of artificial aging time on torsional fatigue life and cyclic behavior of AA6351 aluminum alloy and evaluation of estimation methods. Fatigue Fract Eng Mater Struct. 2023;46(8):2895-908. http://doi.org/10.1111/ffe.14051.
32. Haskel T, Verran GO, Barbieri R, Silva J, Novak D. Effects of strontium addition and T6 heat treatment on uniaxial fatigue of A356 alminum alloy: fatigue life and cyclic behavior. Fatigue Fract Eng Mater Struct. 2022;45(8):2159-73. http://doi.org/10.1111/ffe.13721.
33. Vieira C, Barbieri R, Barbieri MM, Verran GO. Deformation and HCF behavior of A356 aluminum alloys in torsion. Mater Res Express. 2019;6:1165e1.
34. Kohout J, Věchet S. A new function for fatigue curves characterization and its multiple merits. Int J Fatigue. 2001;23(2):175-83. http://doi.org/10.1016/S0142-1123(00)00082-7.
35. Boyer RR, Welsch G, Collings EW, editors. Materials properties handbook: titanium alloys. Materials Park: ASM International; 1994.
36. Meggiolaro MA, Castro JTP, Miranda ACO. Evaluation of multiaxial stress-strain models and fatigue life prediction methods under proportional loading. In: Mattos HSC, Alves M, editors. Mechanics of solids in Brazil. Rio de Janeiro: Brazilian Society of Mechanical Sciences and Engineering; 2009. p. 365-84.
37. Niinomi M. Mechanical properties of biomedical titanium alloys. Mater Sci Eng A. 1998;243(1-2):231-6. http://doi.org/10.1016/S0921-5093(97)00806-X.
38. Sharifimehr S, Fatemi A. Evaluation of estimation methods for shear fatigue properties and correlations with uniaxial fatigue properties for steels and titanium alloys. MATEC Web Conf. 2018;165:4-11. http://doi.org/10.1051/matecconf/201816516012.
39. Nikitin A, Palin-Luc T, Shanyavskiy A, Bathias C. Comparison of crack paths in a forged and extruded aeronautical titanium alloy loaded in torsion in the gigacycle fatigue regime. Eng Fract Mech. 2016;167:259-72. http://doi.org/10.1016/j.engfracmech.2016.05.013.
40. Lee YL, Pan J, Hathaway RB, Barkey ME. Fatigue testing and analysis. Amsterdam: Elsevier; 2005.
41. Haskel T, Verran GO, Barbieri R. Rotating and bending fatigue behavior of A356 aluminum alloy: effects of strontium addition and T6 heat treatment. Int J Fatigue. 2018;114:1-10. http://doi.org/10.1016/j.ijfatigue.2018.04.012.
42. Wang Q, Sun Q, Xiao L, Sun J. Torsion fatigue behavior of pure titanium with a gradient nanostructured surface layer. Mater Sci Eng A. 2016;649:359-68. http://doi.org/10.1016/j.msea.2015.09.104.
43. Qian B, Zhang J, Fu Y, Sun F, Wu Y, Cheng J, et al. In-situ microstructural investigations of the TRIP-to-TWIP evolution in Ti-Mo-Zr alloys as a function of Zr concentration. J Mater Sci Technol. 2021;65:228-37. http://doi.org/10.1016/j.jmst.2020.04.078.
44. Azevedo CRF, Hippert JR. Failure analysis of surgical implants in Brazil: the need for adequate regulation. Public Health Chain. 2002;18:1347-58.
45. Campbell FC. Fatigue and fracture: understanding the basics. Materials Park: ASM International; 2012. http://doi.org/10.31399/asm.tb.ffub.9781627083034.